

## Interaction of Gas-Phase Ozone at 296 K with Unsaturated Self-Assembled Monolayers: A New Look at an Old System

Yael Dubowski, John Vieceli, Douglas J. Tobias,\* Anthony Gomez, Ao Lin, Sergey A. Nizkorodov, Theresa M. McIntire, and Barbara J. Finlayson-Pitts\*

Department of Chemistry, University of California, Irvine, Irvine, California 92697-2025

Received: July 29, 2004; In Final Form: September 2, 2004

The oxidation of organics adsorbed on surfaces by ozone is of fundamental chemical interest and potentially important in the lower atmosphere. Studies of the oxidation of the three-carbon and eight-carbon vinyl-terminated self-assembled monolayers (SAMs, C3= and C8=) on a silicon ATR (attenuated total reflectance) crystal by gas-phase O<sub>3</sub> at 296 K are reported. Oxidation of the SAMs was followed in real time by ATR-FTIR using ozone concentrations that spanned 5 orders of magnitude, from ~10<sup>11</sup> to 10<sup>16</sup> molecules cm<sup>-3</sup>. For comparison, some studies of the saturated C8 SAM were also carried out. The films were also characterized by atomic force microscopy and water contact angle measurements. The loss of C=C and the formation of C=O were measured in real time and shown to be consistent with a Langmuir–Hinshelwood mechanism in which O<sub>3</sub> is rapidly adsorbed on the surface and then reacts more slowly with the alkene moiety. This is supported by molecular dynamics (MD) calculations which show that O<sub>3</sub> does not simply undergo elastic collisions but has a significant residence time on the surface. However, the kinetics measurements indicate a much longer residence time than the MD calculations, suggesting a chemisorption of O<sub>3</sub>. Formaldehyde was observed as a gas-phase product by infrared cavity ring down spectroscopy. Possible mechanisms of the ozonolysis and its atmospheric implications are discussed.

### Introduction

Aerosols play an important role in the chemistry and radiation balance of the atmosphere. They provide surfaces for heterogeneous reactions and affect global climate both directly, by absorbing and scattering solar and terrestrial radiation, and indirectly, by acting as cloud condensation nuclei (CCN).<sup>1–3</sup> Organic matter accounts for a significant portion of the total mass of atmospheric aerosols, in both continental and marine environments.<sup>4,5</sup> These organics are commonly found in the form of mixed aerosols together with inorganic compounds. The organic fraction in mixed aerosols often forms an outer coating over an inorganic core that can be either solid (e.g., mineral dust) or liquid (e.g., aqueous nitrate and sulfate mixtures).<sup>6–8</sup> Reactive uptake of atmospheric trace gases onto such particles may alter the chemical and physical properties of the aerosols. For example, oxidation of an organic aerosol may affect its reactivity toward other trace gases and its hygroscopic properties, in turn affecting the aerosol particles' optical properties and their CCN activity.<sup>2,9,10</sup>

Unsaturated hydrocarbons are widespread in the troposphere.<sup>3</sup> The reaction between unsaturated hydrocarbons and ozone has been studied extensively in the gas phase and in bulk liquids.<sup>3,11,12</sup> More recently, the kinetics and mechanisms of the ozone surface oxidation of condensed alkenes, either as pure liquids (bulk, aerosol particles, and thin films) or adsorbed on solid or liquid substrates have received attention.<sup>9,13–24,67</sup> A common conclusion of these studies is that surface alkenes react with ozone faster than expected based on the analogous gas-phase reactions. In the case of Langmuir films on water, ozone

gets trapped inside the porous network of fluid organic chains on the surface,<sup>13,15</sup> whereas for surfaces of bulk liquids, trapping of ozone on the surface or lowering of the activation energy for the reaction has been suggested.<sup>20,23,24</sup> For alkenes adsorbed on solid substrates, the loss of ozone to the surface has been followed and shown to be faster than expected based on analogous gas-phase O<sub>3</sub>–alkene reactions,<sup>16,20,25</sup> and gas-phase products have been identified.<sup>17</sup> However, in situ real-time monitoring of alkenes adsorbed on solid substrates has only recently been reported.<sup>26</sup> This is important, because ozone has been shown to physisorb on some organics as the initial step in a multistep mechanism.<sup>22,27</sup> In such a case, loss of gas-phase ozone may not occur at the same rate as formation of products on the surface and representation of reactions by a single value for the reaction probability under all conditions may not be appropriate.

In the present study, alkylsilane self-assembled monolayers (SAMs) were used as proxies for organics adsorbed on solid substrates such as airborne dust particles or urban surfaces (e.g., buildings).<sup>28–30</sup> The SAMs were attached directly to the surface of an attenuated total reflection (ATR) crystal, and their oxidation by gaseous ozone (10<sup>11</sup>–10<sup>16</sup> molecules cm<sup>-3</sup>) was monitored in real time using FTIR at 1 atm pressure and room temperature (296 ± 2 K). Although the reactions of ozone with a variety of alkene SAMs on silica surfaces have been previously studied,<sup>16,17,20</sup> kinetics measurements of the condensed phase oxidation in real time have not been reported previously. In addition to the real-time FTIR monitoring of the surface, gas-phase products of the ozonolysis of SAMs were probed by infrared cavity ring-down spectroscopy (IR-CRDS). The surfaces were characterized additionally by atomic force microscopy (AFM), and changes in their hygroscopicity upon oxidation were probed using contact angle measurements. Finally, molecular

\* To whom correspondence should be addressed. B. J. Finlayson-Pitts (949) 824-7670, e-mail bjfinlay@uci.edu; D. J. Tobias (949) 824-4295, e-mail dtobias@uci.edu.

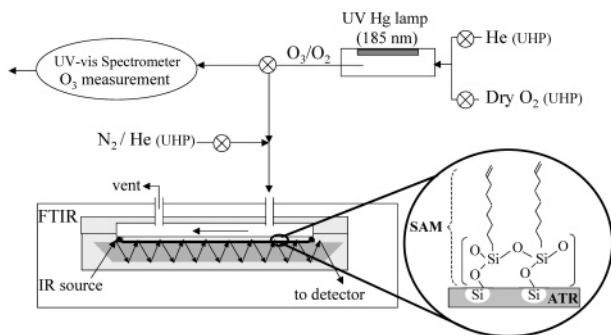


**Figure 1.** Schematic diagram of the flow system in the oxidation experiments.

dynamics simulations were used to investigate the nature of these SAMs and their physical interaction with gaseous ozone. The combination of all of these approaches yields new molecular level insights into the interaction of  $O_3$  with unsaturated SAMs. Specifically, we show that the mechanism involves the initial adsorption of  $O_3$  on the SAM followed by a slower reaction with the double bond. The atmospheric implications are discussed.

## Experimental Section

**1. Deposition of SAMs.** Three different alkylsilanes were used to form SAMs on silica substrates: (1) methyl-terminated *n*-octyltrichlorosilane, C8 (Gelest, 95%); (2) vinyl-terminated allyltrimethylchlorosilane, C3= (Aldrich, 95%); (3) vinyl-terminated 7-octenyltrichlorosilane, C8= (United Chemicals Technologies, 95%). The SAMs were deposited directly on a  $45^\circ$  Si ATR crystal ( $8\text{ cm} \times 1\text{ cm} \times 0.4\text{ cm}$ , 10 reflections) according to a well-established technique.<sup>31</sup> Briefly, the crystal was cleaned with boiling ethanol and then with boiling chloroform. The dry crystal was further cleaned for ca. 30 min with an argon (Oxygen Services Co., ultrahigh purity (UHP), >99.999%) plasma discharge (Harrick Scientific Plasma Cleaner/Sterilizer PDC-32G, medium power). Upon removal from the plasma cleaner, the substrate was rinsed with Nanopure water (18 M $\Omega$  cm) to hydrate the surface and then dried with a flow of  $N_2$  (Oxygen Services Co., UHP, 99.999%). The Si crystal is known to have a layer of silica on it under these conditions. To coat only the crystal area that is exposed to ozone during the experiments, the deposition of the SAM was carried out with the dried crystal placed in a fabricated Teflon holder. The latter was designed to have an open slot on its top side with identical geometry (area of  $3.6\text{ cm}^2$ ) to the one in the horizontal ATR holder used during the experiments. About 2 mL of a millimolar solution of alkylsilane in hexadecane (Aldrich, 99%) was introduced onto the slot for ca. 10 min, during which time the SAM deposited on the crystal. The SAM-coated crystal was then placed in boiling chloroform to remove any unreacted physisorbed alkylsilane. The coating and chloroform extraction steps were repeated two additional times to ensure a smooth, closely packed coating, which was characterized as described below. Samples prepared for AFM imaging and cavity ring-down spectroscopy (see below) were deposited on Si wafers following the same procedure and were stored under dry  $N_2$  until analysis.

**2. Reaction with  $O_3$ .** After placement of the Si crystal in a flow-through horizontal ATR holder (Pike Technologies), the system was thoroughly purged with dry nitrogen overnight. A schematic diagram of the experimental flow system is shown in Figure 1. Ozone was generated by irradiating a dry flow of  $O_2$  (Oxygen Services Co., UHP, >99.993%) with a low-pressure

mercury lamp (Jelight company Inc., Double Bore 78-2046); the 185 nm line causes dissociation of  $O_2$  to generate  $O(^3P)$  that adds to  $O_2$ , generating  $O_3$ . The  $O_3$  concentration in the mixture was controlled by varying the exposure of oxygen gas to the UV light using an adjustable opaque sleeve surrounding the UV lamp. The  $O_3/O_2$  mixture was introduced into a 5-cm cell with quartz windows, and the  $O_3$  concentration was determined using a UV-vis spectrometer (Hewlett-Packard model 8452A) based on its absorption at 254 nm ( $\sigma = 1.15 \times 10^{-17}\text{ cm}^2\text{ molecule}^{-1}$ , base *e*).<sup>32</sup> Before each experiment, the  $O_3/O_2$  mixture was flowed through the lamp compartment and the UV-vis spectrometer for over an hour to ensure that the ozone concentration was stable. The gas flow was then diluted with  $N_2$  and introduced into the ATR cell whose headspace is  $\sim 500\ \mu\text{L}$ . The stainless steel parts of the ATR cell were coated with halocarbon wax, and the lines were Teflon, materials for which there is very little loss of  $O_3$  and for which preconditioning is therefore not required. In the experiments with  $[O_3] < 10^{14}\text{ molecules cm}^{-3}$ , a mixture of  $O_2$  in He (Oxygen Services Co, UHP, >99.995%) was irradiated and then further diluted with He downstream. The  $O_3$  concentration in the cell was calculated from that in the  $O_3/O_2$  mixture and the factor by which it was diluted with  $N_2$  or He. In the experiments with  $[O_3] \approx 10^{11}\text{ molecules cm}^{-3}$ , the ozone mixture was introduced into the ATR system by withdrawing it (at  $\sim 30\text{ cm}^3\text{ min}^{-1}$ ) from a premixed collapsible Teflon chamber. As discussed below, the effective reaction probability for  $O_3$  with the SAMs, although larger than that for analogous gas phase reactions, is, on an absolute scale, relatively small. Under our conditions, the loss of  $O_3$  in the ATR cell is calculated to be less than 5% of its initial concentration so that there should not be significant gradients of ozone along the crystal. In any case, the ATR measurements average over the entire length of the crystal so that the reported reaction probabilities reflect that from an average concentration of  $O_3$  in the cell.

A background spectrum of the surface was taken before introducing the  $O_3/O_2$  mixture into the ATR cell. Sample spectra of the surface were recorded approximately every 40 s during exposure to ozone, averaging 64 scans with a resolution of  $4\text{ cm}^{-1}$  using an FTIR spectrometer (Cygnus 100, Mattson). Over the spectral range of interest,  $1500\text{--}4000\text{ cm}^{-1}$ , the penetration depth ( $d_p$ ) of the evanescent wave into the ATR surrounding in the present experimental system was calculated (eq I) to be  $0.5\text{--}0.2\ \mu\text{m}$ , respectively.<sup>33</sup>

$$d_p = \frac{\lambda}{n_1 2\pi(2 \sin^2 \theta - n_{21}^2)^{1/2}} \quad (\text{I})$$

In eq I,  $\lambda$  is the wavelength of the light,  $n_1$  is the refractive index of the denser medium (3.4 for the Si ATR crystal),  $\theta$  is the incident angle, and  $n_{21}$  is the ratio between the refractive index of the rarer medium ( $n_2$ ) and the crystal ( $n_1$ ). In the case of a thin film, the refractive indices of the ATR crystal and of the media above the film control the electric field more than the refractive index of the film itself; therefore  $n(\text{air})$  was taken as  $n_2$ .<sup>33</sup> This depth is much larger than the estimated height of the studied SAMs ( $\sim 13$  and  $7\ \text{\AA}$  for C8= and C3=, respectively), and hence the ATR-IR spectra of these SAMs should resemble their transmission spectra.<sup>33</sup>

As discussed below, exposure of the reacted SAMs to gaseous ammonia was used to probe for the generation of carboxylic acids in the reaction. Ammonia vapor was collected over an  $NH_4OH$  solution (29.5%, Fisher) after two cycles of freeze-

pump–thaw. The glass cell containing 401 Torr of ammonia vapor (at 23 °C, including 18 Torr of water vapor) was then flushed into the ATR system with a flow of nitrogen at 1 atm.

**3. Atomic Force Microscopy (AFM) Imaging.** Specimens were imaged in air at ambient pressure and humidity by tapping mode using a Park Scientific AutoProbe CP scanning probe microscope equipped with a piezoelectric scanner with a range up to 10  $\mu\text{m}$ . The scanner was calibrated in the  $xy$  directions using a 1.0  $\mu\text{m}$  grating and in the  $z$  direction using several conventional height standards such as highly oriented pyrolytic graphite. The tips employed were V-shaped silicon 2  $\mu\text{m}$  cantilevers (Ultralevers, model no. ULNC-AUNM, Thermo-Microscopes) or ultrasharp V-shaped noncontact silicon (Ultrasharp cantilevers, model no. NSC11, MikroMasch). Topographs were obtained as  $256 \times 256$  pixels and were flattened line by line and analyzed using AutoProbe image processing software supplied by the manufacturer of the AFM. The root-mean-square (rms) surface roughness was calculated from  $R_{\text{rms}} = [\sum^N (z_N - \bar{z})^2 / (N - 1)]^{1/2}$  where  $\bar{z}$  is the average  $z$  height and  $N$  is the number of points sampled.

**4. IR-CRDS Spectroscopy.** The gas-phase products of the ozonolysis of SAMs were probed in a separate experiment using IR-CRDS. Commercial Si(111) wafers optically polished on one side were used as substrates for SAMs. The SAM-coated wafers were placed inside a vacuum chamber just below the axis of the CRDS cavity, where they were exposed to ozone at a concentration of  $\sim 10^{14}$  molecules  $\text{cm}^{-3}$ . The CRDS cavity was equipped with 99.98% reflective mirrors optimized for the 3.3  $\mu\text{m}$  range (Los Gatos Research). The cavity mirrors were spaced by about 60 cm and protected by a constant purging flow of dry helium, resulting in empty cavity ring-down times of the order of 5–10  $\mu\text{s}$ . A commercial pulsed optical parametric oscillator laser (0.1  $\text{cm}^{-1}$  spectral resolution) was used to optically pump the cavity. The region between 2910 and 2930  $\text{cm}^{-1}$ , which contains easily identifiable lines of formaldehyde and formic acid, was used to detect these two products. All experiments were carried out at room temperature (295 K) under slow flow conditions in an atmosphere of mostly helium at 50–130 Torr. An optoacoustic reference spectrum of HCOOH was recorded in parallel with CRDS spectra for wavelength calibration purposes.

**5. Contact Angle Measurements.** The surface wettability of the SAM-coated crystal was probed before and after exposure to  $\text{O}_3$  via contact angle measurements using water droplets. Quasi-equilibrium contact angles of 1  $\mu\text{L}$  Nanopure water sessile droplets were measured under ambient conditions with a Kodak DCS 315 camera equipped with a long-range microscope (Infinity Optics). The shape of the droplet depends on its interaction with the surface.<sup>34</sup> The line tangent to the curve of the droplet at the point where it intersects the solid surface forms the contact angle. A water droplet resting on a hydrophobic surface would form a spherical droplet having a high contact angle, but it would have a much smaller contact angle when placed on a more hydrophilic surface.

**6. Molecular Dynamics Simulations.** Molecular dynamics simulations were carried out to provide insight into the experimental results. The SAMs used in the simulations were alkylthiolates because the surface potentials for these are well developed.<sup>35</sup> This is justified because experimental data from the literature suggest that the structural differences between SAMs composed from long alkane chains on silica and on gold are minor. For example, the spacing between Si atoms on a silica surface is 4.97 Å whereas the S atoms on a gold surface are 4.4 Å apart.<sup>36</sup> Also, the thickness and tilt angle of alkane

SAMs on a silica surface differ only slightly from SAMs of similar carbon length on a gold surface.<sup>37,38</sup> On a silica surface, the thickness and tilt angle of a SAM composed from octadecyltrichlorosilane (18 carbons long) is 25.2 Å and 10°, respectively.<sup>37</sup> On a gold surface, the thickness of a SAM composed from hydrocarbons that are 18 alkane carbons long is 29 Å and the tilt angle of chains with 16–22 alkane carbons is 20–30°.<sup>38</sup>

*a. The Neat Systems.* Molecular dynamics simulations were performed for two different SAMs in order to characterize their structures. Each SAM consisted of either 64 1-propenethiolate ( $\text{CH}_2=\text{CHCH}_2\text{S}$ ) molecules or 64 1-octenethiolate ( $\text{CH}_2=\text{CH}(\text{CH}_2)_6\text{S}$ ) molecules, where the sulfur atom was chemisorbed to a gold (111) surface. The simulation box dimensions were  $x = 40.08$  Å,  $y = 34.72$  Å, and  $z = 56.00$  Å for the 1-propenethiolate SAM and  $x = 40.08$  Å,  $y = 34.72$  Å, and  $z = 62.00$  Å for the 1-octenethiolate SAM. The  $z$  dimension was perpendicular to the SAM/vapor interface, and its magnitude was reduced with a shorter hydrocarbon chain to make the gas-phase volume the same in both systems. The gold surface was located at  $z = 0$  Å in both systems. The simulation box geometry resulted in a surface area of 22 Å<sup>2</sup> molecule<sup>-1</sup>. The force field for the hydrocarbons was taken from previously published work.<sup>39</sup> An adsorption potential and surface corrugation potential were included in the simulations, following the work of Mar and Klein.<sup>35</sup>

*b. Ozone.* Molecular dynamics simulations of the SAMs described above in the presence of ozone were performed in order to characterize the adsorption of ozone to the SAM surfaces and the collision rate between ozone molecules and double bonds. The oxygen atoms of ozone were described using the CHARMM22 force field,<sup>40</sup> where each oxygen atom was considered to be a carbonyl oxygen atom with no atomic charges (the hybridization in ozone is more similar to that of a carbonyl oxygen atom,  $\text{sp}^2$ , than to that of an oxygen in an alcohol or water,  $\text{sp}^3$ ). The electrostatic interactions were ignored in these systems because the hydrocarbon molecules that compose the SAMs were nonpolar and the molecular dipole moment of ozone is known from experiment to be small (0.53 D).<sup>41,42</sup> The gas-phase equilibrium geometry was used for the ozone molecules, where the two bond lengths were 1.278 Å and the bond angle was 117°.<sup>43</sup> A reflecting wall was included to prevent the escape of gas-phase ozone molecules. It was placed in the  $xy$  plane at  $z = 56$  Å in the 1-propenethiolate SAM and at  $z = 62$  Å in the 1-octenethiolate SAM.

*c. Simulation Details.* After 400 ps equilibrations, 800 ps simulations of the neat systems were performed. Then, four ozone molecules were added to the final configuration from the simulation of each neat system. The ozone molecules were placed approximately 20 Å above the SAM surfaces, and 300 ps equilibrations were run. After equilibration, the SAMs with ozone were simulated for 1600 ps. All of the simulations were performed with a constant number of molecules, temperature, and volume using CHARMM.<sup>44</sup> The system temperature of 300 K was controlled using Nose–Hoover chain thermostats.<sup>45</sup> The van der Waals interactions were truncated at 10 Å. A 1.0 fs integration time step was used, and all bonds lengths involving hydrogen atoms were constrained using the SHAKE/RATTLE algorithm.<sup>46,47</sup>

## Results and Discussion

Deposition of SAMs directly on an ATR crystal enables detection of various features of even very short monolayers (e.g.,  $\text{C}3=$ ) and permits real-time monitoring of these features during

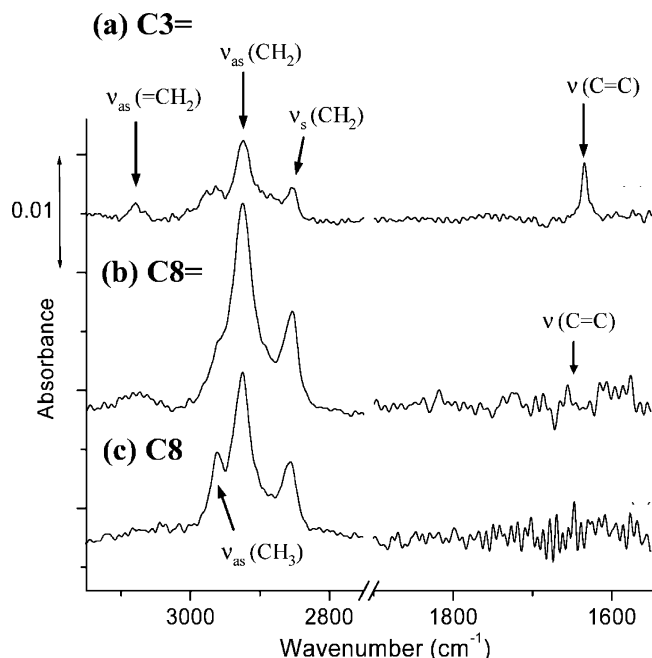


**Figure 2.** ATR-FTIR spectra of the three SAMs before exposure to ozone. The spectra shown were obtained by coating the ATR crystal with the SAM on all sides.

experiments. Typical ATR-FTIR spectra of the three unreacted SAMs used in the present study are shown in Figure 2. The absorption bands at  $\sim 2856$  and  $\sim 2926$   $\text{cm}^{-1}$  are due to the  $-\text{CH}_2$ -symmetric ( $\nu_s$ ) and asymmetric ( $\nu_{as}$ ) stretches, respectively.<sup>48</sup> The additional band at  $\sim 2962$   $\text{cm}^{-1}$  in the spectrum of the saturated C8 SAM is assigned to the asymmetric stretch of the methyl groups ( $\nu_{as} -\text{CH}_3$ ).<sup>48</sup> These peaks are in excellent agreement with previous studies on similar monolayers<sup>16,17</sup> and are indicative that the chains are not as highly ordered as longer chain alkane SAMs.<sup>49,50</sup> The terminal vinyl groups in C3= and C8= give rise to two additional bands: (1) a  $=\text{CH}_2$  asymmetric stretch at  $\sim 3081$   $\text{cm}^{-1}$  for C3= and at  $\sim 3077$   $\text{cm}^{-1}$  for C8=, and (2) a C=C stretch at  $\sim 1635$   $\text{cm}^{-1}$  (C3=) and at  $\sim 1642$   $\text{cm}^{-1}$  (C8=). The C=C stretch has a much lower intensity in the spectrum of C8= than that in the C3= spectrum. The lower relative intensity of the C=C band in the C8= SAM may be indicative of a more highly ordered film formed with longer alkyl chains (where van der Waals forces assist in forming highly ordered films). The C=C stretch vibrations in well-oriented SAMs are mainly perpendicular to the surface, an orientation to which ATR is not sensitive.<sup>33,51,52</sup> Thus, a more highly ordered SAM for C8= may lead to a reduced intensity of the C=C band.

To probe this, molecular dynamics (MD) simulations were carried out to examine the orientation of the chains and of the terminal vinyl groups relative to the surface normal. Snapshots of the neat C3= and C8= SAM simulations are shown in Figure 3. The top views are looking in the  $z$  dimension from the airside of the interface. The thickness of the simulated SAMs is approximately 7 Å for the C3= SAM and 13 Å for the C8= SAM, which is in excellent agreement with experimental measurements of alkythiol SAM thickness using ellipsometry.<sup>38</sup>

The probability distributions of tilt angles and double bond orientations from the simulations are shown in Figure 4. In Figure 4a, the tilt angle distribution, based on the angles between the surface normal and the S-C1 bond, spans the range from  $0^\circ$  to approximately  $30^\circ$  for the C8= system. However, in the C3= system, the tilt angles can be much larger (up to about

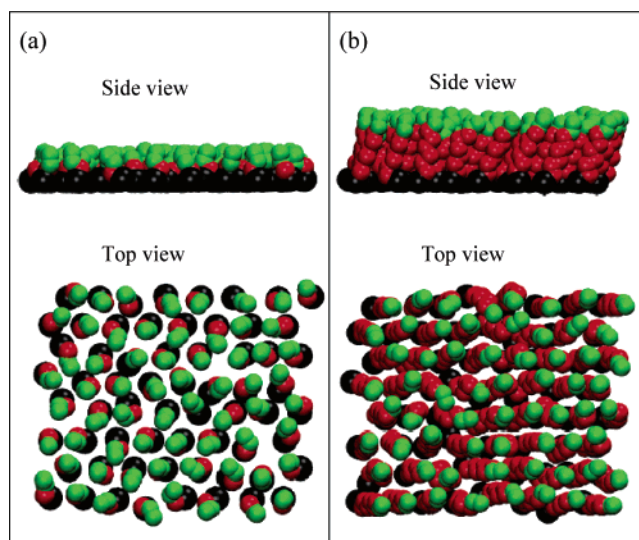


**Figure 3.** Snapshots from the molecular dynamics simulations of (a) 1-propenethiolate and (b) 1-octenethiolate SAMs. Sulfur atoms are shown in black, alkane carbons in red, and alkene carbons in green.

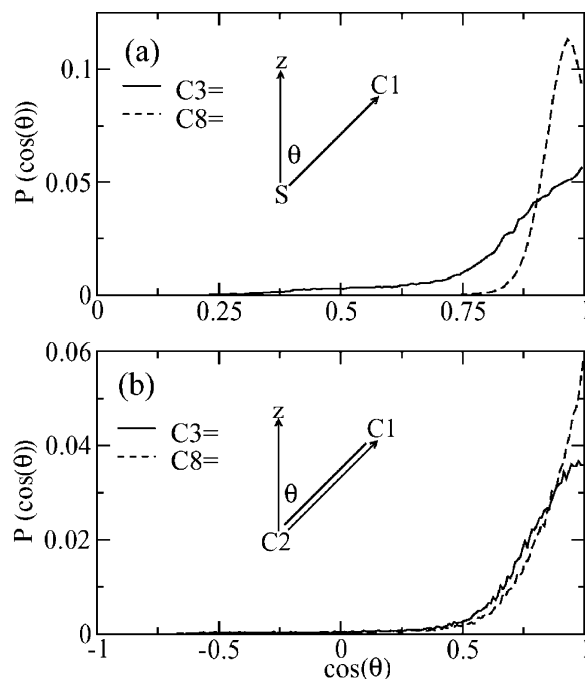


**Figure 4.** Probability density distributions from the molecular dynamics simulations of the angle,  $\theta$ , between the surface normal and the (a) S-C1 bond and the (b) C=C bond, in both C8= (dashed line) and C3= (solid line).

$70^\circ$ ). This broader distribution of tilt angles for the C3= SAM relative to the C8= SAM demonstrates that there is a greater degree of disorder in the C3= SAM. The observation of increasing disorder with decreasing chain length has been observed previously with both alkythiol SAMs on gold<sup>38</sup> and alkylsilane SAMs.<sup>52</sup> In Figure 4b, the double bond orientation distributions, defined as the distribution of angles between the surface normal and the terminal C=C, are shown. Although the overall distributions are quite similar, the C8= SAM has somewhat more double bonds oriented perpendicular to the interface. This suggests that better ordering of the C8= SAM makes a contribution to the different relative intensities observed for the C=C and  $-\text{CH}_2-$  bands in the two SAMs.

Further evidence supporting the increased order for the C8= SAM involves measurements of the contact angles for water

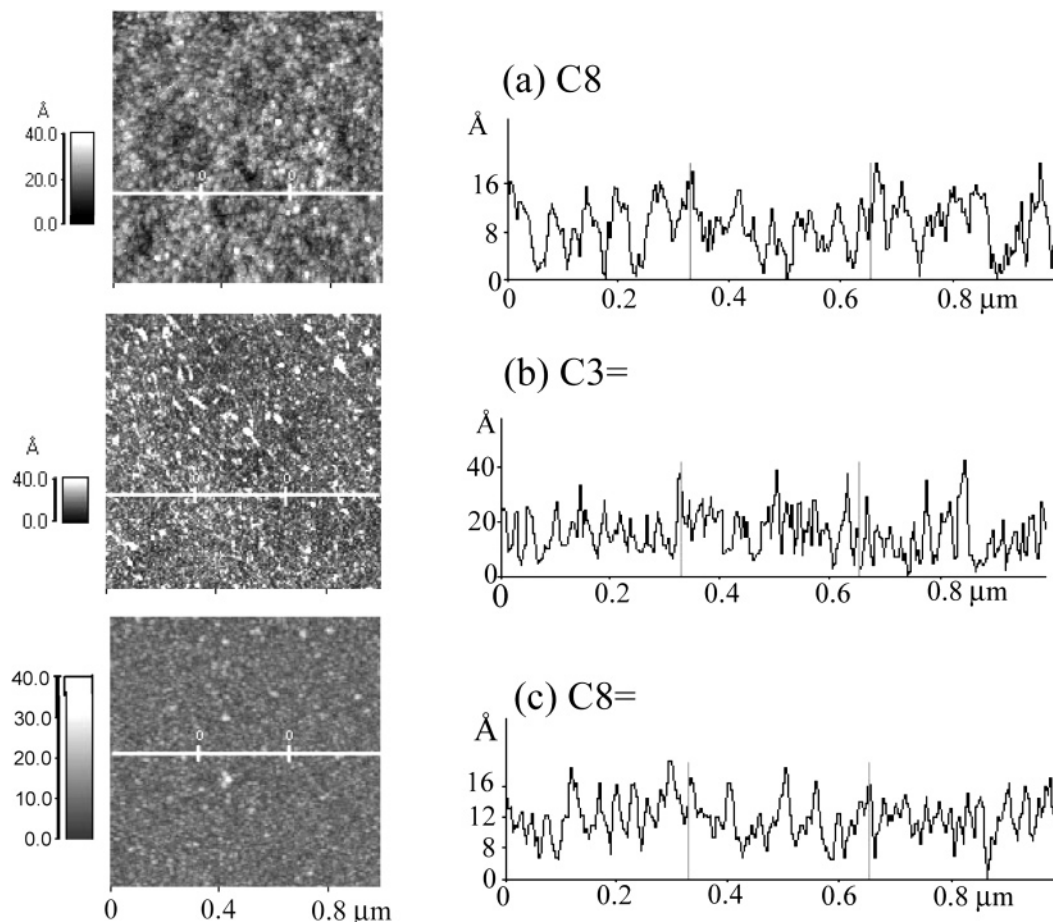


**Figure 5.** AFM images of (a) C8, (b) C3=, (c) C8= SAMs deposited on Si wafers. Cross sectional profiles measured along lines shown in the figures are presented on the right.

and AFM imaging of these SAMs. For the unreacted C8= SAM, the contact angles were in the range of 89° to 96° compared to 77° to 84° for the C3= SAM, and around 100° for the saturated C8 SAM ( $1\sigma$  for these measurements is 2°). These values are lower than those reported for saturated long-chain SAMs that are highly ordered ( $\sim 110^\circ$ ),<sup>53</sup> indicating that the unsaturated SAMs form a more disordered layer, as might be expected. The contact angles reported in the present study are in good agreement with previous measurements on similar SAMs<sup>17,54</sup> and with the trend of the tilt angle distributions from the MD simulations.

AFM images of the various SAMs, deposited on Si wafers, are shown in Figure 5. The averaged rms roughness values measured were 6.5, 3.1, and 4.2 Å for C3=, C8=, and C8, respectively. These low roughness values suggest that all three of the SAMs used here make relatively uniform films. In the case of C3=, the AFM image shows the presence of small aggregates, which are most likely due to polymerization of the C3= chains. This is in agreement with the unrealistically high surface density obtained for these SAMs based on their IR absorption (see below), as the ATR measures these polymerized chains as well.

The FTIR spectra of the SAMs shown in Figure 2 were obtained by ratioing the spectra of the SAMs to that of the clean crystal; water vapor contributions due to changing purge in the sample compartment of the spectrometer were also subtracted. The noise in those spectra is on the order of  $7 \times 10^{-4}$  ( $3\sigma$ ) and arises primarily from small changes in the positioning of the ATR crystal between the background spectrum of the clean crystal and that of the reinserted, coated crystal. In addition,

opening the sample compartment led to increased water vapor in the light path.

In the oxidation experiments, however, the noise was significantly improved ( $3\sigma \sim 1 \times 10^{-4}$ ), which allowed changes even in the weak C=C band in C8= to be measured during the oxidation. For example, as seen in Figure 6, a clear decrease in the absorption bands associated with the terminal vinyl groups is observed for both the C3= and the C8= along with a simultaneous increase in a broad peak centered at  $\sim 1710 \text{ cm}^{-1}$  (for C3=) and at  $1728 \text{ cm}^{-1}$  (for C8=) that is indicative of the formation of a carbonyl group. The improved signal-to-noise ratio was achievable by purging the system overnight with the coated ATR mounted in the sample compartment to minimize changes in water vapor and by using the spectrum of the SAM before exposure to  $\text{O}_3$  as the reference, rather than the spectrum of the clean crystal. The improved signal-to-noise ratio obtained in this manner thus allows the oxidation of the SAMs to be followed in real time with high sensitivity.

The width of the carbonyl peak for the oxidized C3= SAM is about twice that for the oxidized C8= SAM. This may be because of two factors. First, as discussed above, there is evidence that the unreacted C3= SAM is initially less ordered than the C8= SAM, and hence its oxidized form would be expected to be less ordered as well. Both the positions and the bandwidths are known to shift as a SAM becomes more disordered; for example, the bandwidth for the  $\nu_{\text{as}}(\text{CH}_2)$  band of a tightly packed octadecyltrichlorosilane SAM is  $16 \text{ cm}^{-1}$  but  $\sim 25 \text{ cm}^{-1}$  for less highly ordered films.<sup>50</sup> Second, it may be indicative of the presence of comparable amounts of both aldehyde and carboxylic acid products on the surface. Thus,

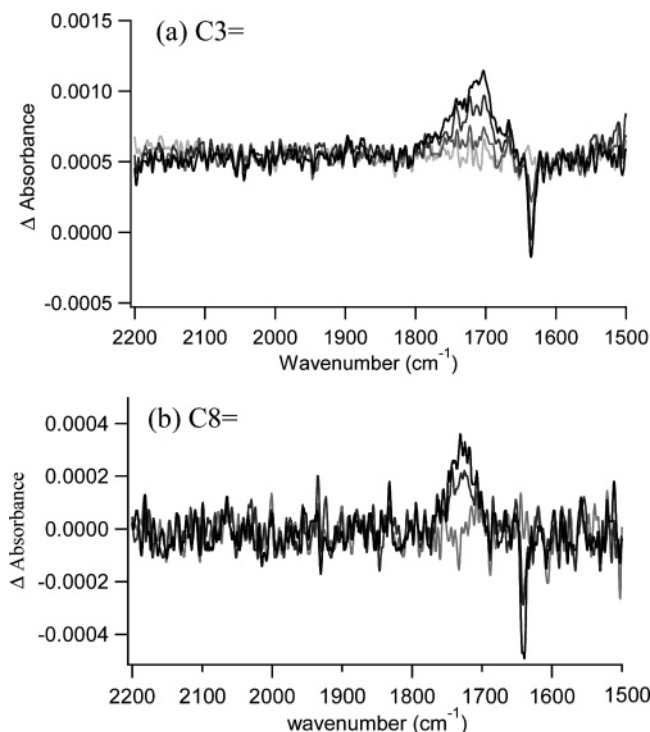


**Figure 6.** Typical changes in the absorption spectra of (a) C3= and (b) C8= SAMs upon exposure to ozone ( $8 \times 10^{14}$  molecules  $\text{cm}^{-3}$ ). Spectra were recorded at progressive ozone exposure times (light gray to black, respectively), for C3= 0, 0.5, 1, and 5 min; for C8= 0, 1, and 6 min.

the carbonyl peak for aldehydes is blue-shifted by about  $20 \text{ cm}^{-1}$  compared to that for acids ( $\sim 1730$  versus  $1710 \text{ cm}^{-1}$ ). This possibility is discussed in more detail below in conjunction with the IR-CRDS results on the gas-phase products.

**Kinetics.** As seen in Figure 7, the C=O peak increases (Figure 7a) and the C=C band decreases (Figure 7b) in the first few minutes upon exposure to ozone. No such pattern was observed for the saturated C8 SAM, as expected based on the very low reactivity of alkanes toward ozone.<sup>3,11,12</sup> Because the product C=O absorbance is linearly correlated to its surface coverage, the following should hold

$$\frac{\text{abs}(\text{C}=\text{O})_t}{\text{abs}(\text{C}=\text{O})_\infty} = \frac{[\text{C}=\text{O}]_t}{[\text{C}=\text{O}]_\infty} \quad (\text{II})$$

where  $\text{abs}(\text{C}=\text{O})_t$  and  $[\text{C}=\text{O}]_t$  represent the C=O absorbance and the total surface concentration of C=O groups at time  $t$ , respectively, and  $t = \infty$  represents the time at which the SAM is fully oxidized. Because in a completely oxidized SAM  $[\text{C}=\text{O}]_\infty$  is expected to be equal to the surface density of the original monolayer,  $[\text{SAM}]_0$ , this correlation can be expressed as

$$[\text{C}=\text{O}]_t = \frac{\text{abs}(\text{C}=\text{O})_t \times [\text{SAM}]_0}{\text{abs}(\text{C}=\text{O})_\infty} \quad (\text{III})$$

$$\left(\frac{d[\text{C}=\text{O}]}{dt}\right)_t = \left(\frac{d[\text{abs}(\text{C}=\text{O})]}{dt}\right)_t \times \frac{[\text{SAM}]_0}{\text{abs}(\text{C}=\text{O})_\infty} \quad (\text{IV})$$

The initial surface densities of the SAMs were estimated based on the absorbance of the  $-\text{CH}_2-$  asymmetric stretch at  $\sim 2926 \text{ cm}^{-1}$  (after deconvoluting the spectra and normalizing the absorption to the number of reflections along the ATR crystal), using the nonpolarized ATR measurements reported

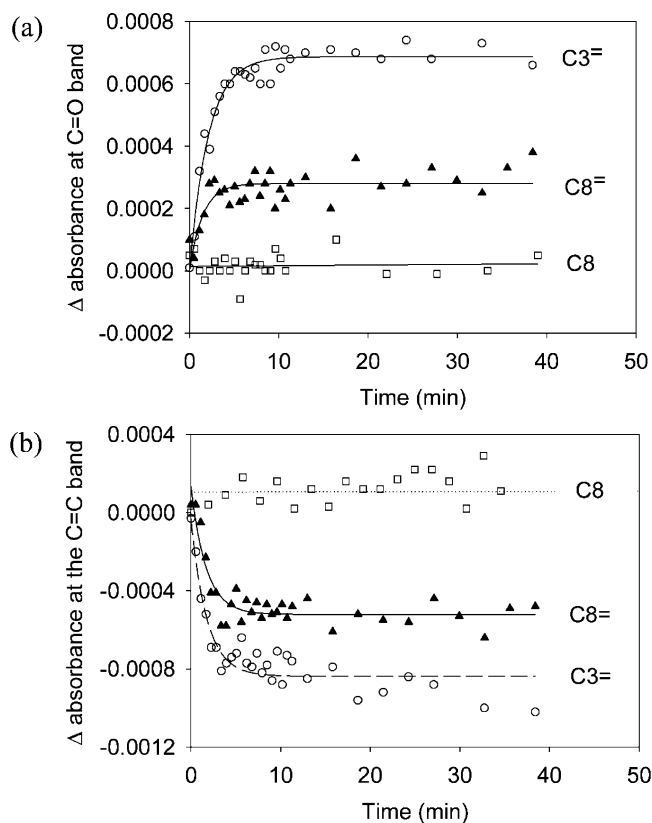


**Figure 7.** Changes in absorbance at the (a) C=O and (b) C=C bands as a function of exposure time to  $\text{O}_3$  ( $8 \times 10^{14}$  molecules  $\text{cm}^{-3}$ ), for C3= (open circles), C8= (solid triangles), and C8 (open squares).

by Maoz and Sagiv<sup>51</sup> for longer SAMs on silicon (absorbance = 0.00021 per  $\text{CH}_2$  group per ATR reflection) and the surface density for such well-packed SAMs ( $4.2 \times 10^{14}$  molecules  $\text{cm}^{-2}$ ).<sup>55,56</sup> The average surface density was calculated to be  $(3.1 \pm 0.5) \times 10^{14}$  ( $1\sigma$ ) molecules  $\text{cm}^{-2}$  for both the C8= and C8 SAMs. Given a typical surface density of free OH groups on the silica surface to be  $\sim 4.5 \times 10^{14}$  molecules  $\text{cm}^{-2}$ ,<sup>57,58</sup> this suggests occupation of about 70% of the binding sites. The values obtained for surface densities of C3= were higher with a larger uncertainty,  $(8 \pm 4) \times 10^{14}$  molecules  $\text{cm}^{-2}$ ; this may be due to the higher disorder of the C3= SAM, as well as the presence of some polymerized aggregates as indicated by the AFM image (Figure 5). Therefore, we chose to use for C3= the same surface density that was calculated for C8 and C8=. The rate of change of the C=O absorbance,  $d[\text{abs}(\text{C}=\text{O})]/dt$ , was calculated using the derivative of the best fit to the experimental absorbance data (Figure 7a). Because active surface sites are consumed during the reaction, only the initial rates were considered.

Gas-surface reactions are normally treated in terms of a reaction probability ( $\gamma$ ), defined as the fraction of collisions of gas with the surface that lead to reaction. In this framework, the rate of formation of C=O per  $\text{cm}^2$  is given by eq V

$$\left(\frac{d[\text{C}=\text{O}]}{dt}\right)_t = \gamma \times [\text{O}_3]_g \sqrt{\frac{RT}{2\pi M}} \quad (\text{V})$$

where  $[\text{O}_3]_g$  is the gas-phase ozone concentration adjacent to the surface,  $R$  is the gas constant,  $T$  is the temperature, and  $M$  is the molecular weight of ozone. This assumes that diffusion of  $\text{O}_3$  to the surface is not a limiting factor; given the fact that the measured reaction probabilities are small,  $\leq 10^{-5}$ , and that

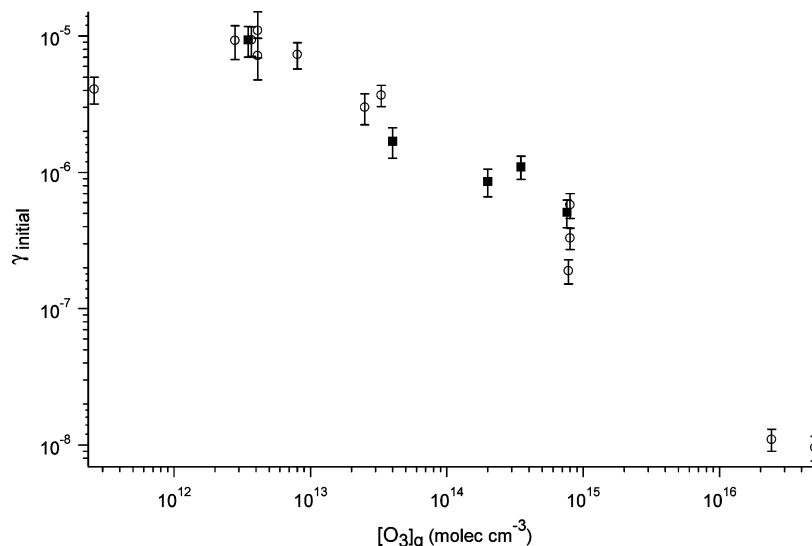


**Figure 8.** Calculated initial reaction probabilities,  $\gamma_{\text{initial}}$ , for the oxidation of C3= (open circles) and C8= (solid squares) as a function of the gas-phase ozone concentration. The data points were calculated using eq VI based on measured values of the carbonyl absorbances and initial  $\text{O}_3$  and SAM concentrations.

the cell geometry is expected to favor turbulent flow, this assumption is reasonable. Combining eqs IV and V gives an expression for  $\gamma$  in terms of the measured experimental parameters, eq VI

$$\gamma = \left( \frac{d[\text{abs}(\text{C}=\text{O})]}{dt} \right)_t \times \frac{[\text{SAM}]_0}{\text{abs}(\text{C}=\text{O})_{\infty} [\text{O}_3]_g \sqrt{RT/2\pi M}} \quad (\text{VI})$$

Because the reaction rate (i.e., molecules  $\text{cm}^{-2} \text{s}^{-1}$  of product formed) changes linearly with the gas-phase ozone concentration, the reaction probability is expected to be independent of  $[\text{O}_3]_g$ .

Figure 8 shows the values of the initial reaction probabilities,  $\gamma_{\text{init}}$ , calculated from eq VI as a function of the gas-phase ozone concentration (note the log–log scale). The error bars, typically of the order of 20%, are the statistical errors only (1  $\sigma$ ) and do not include potential systematic errors. The greatest uncertainty is in the initial surface concentration of the SAM, which can vary from one coating to another; in addition, the value for the SAM surface concentration is based on the absorption coefficient for  $-\text{CH}_2-$  groups reported by Maoz and Sagiv<sup>51</sup> for a C18 SAM, which was assumed to apply to our C3 and C8 SAMs. We estimate that inclusion of such potential systematic errors could lead to an overall error for an individual experiment of the order of 50%. However, it is clear that  $\gamma_{\text{init}}$  is inversely and nonlinearly dependent on  $[\text{O}_3]_g$  and levels off as the ozone concentration approaches  $10^{11} \text{ cm}^{-3}$ . The overall error associated with the point at the smallest ozone concentration may be larger than those at higher concentrations due to the longer duration of the exposure,  $\sim 17 \text{ h}$ , during which a greater variation in the experimental conditions (e.g.,  $\text{O}_3$  concentration) would be expected. Thus, when these factors are taken into account, the data point at the lowest  $\text{O}_3$  concentration is consistent with a leveling off of the measured reaction probability.

Because these reaction probabilities are calculated for  $t \rightarrow 0$ , passivation of the surface by reaction of a significant fraction of the alkene groups cannot be responsible for this dependence of the reaction probability on ozone. Consistent with this, the initial product formation was accompanied by corresponding decreases in the C=C peaks, which would not be the case if

the surface had been rapidly oxidized before the first FTIR scans were completed and the measurements of reaction probabilities were made during further oxidation of the initial products.

Clearly, treating the reaction of gas-phase  $\text{O}_3$  with the unsaturated SAMs as a simple collision with the surface that has a fixed probability of reaction does not adequately describe the experimental data. An alternative is a multistep process in which  $\text{O}_3$  is first physisorbed onto the surface and hence has a finite residence time on the SAM before reacting. Reaction of  $\text{O}_3$  with the SAM then occurs in competition with its desorption from the surface. This is the well-known Langmuir–Hinshelwood type of mechanism.<sup>59,60</sup>

Assuming that ozone cannot be adsorbed onto a previously adsorbed ozone, then the rate of adsorption ( $R_a$ ) and rate of desorption ( $R_d$ ) of ozone can be expressed in the form of eqs VII and VIII

$$R_a = k_a [\text{O}_3]_g ([S] - [\text{O}_3]_s) \quad (\text{VII})$$

$$R_d = k_d [\text{O}_3]_s \quad (\text{VIII})$$

where  $k_a$  is the adsorption rate constant ( $\text{cm}^3 \text{ molecules}^{-1} \text{ s}^{-1}$ ),  $[S]$  is the total surface density of  $\text{O}_3$  adsorption sites (taken as  $5 \times 10^{14} \text{ molecules cm}^{-2}$  for ozone),  $[\text{O}_3]_s$  is the surface density of adsorbed ozone (molecules  $\text{cm}^{-2}$ ), and  $k_d$  is the desorption rate constant ( $\text{s}^{-1}$ ). At equilibrium, the two rates are equal, and the steady-state ozone coverage on the surface can be written as

$$[\text{O}_3]_s = \frac{k_a [\text{O}_3]_g [S]}{k_a [\text{O}_3]_g + k_d} = \frac{[\text{O}_3]_g [S]}{[\text{O}_3]_g + B} \quad (\text{IX})$$

where  $B = k_d/k_a$ . In the present system, the surface reaction rate (molecules  $\text{cm}^{-2} \text{ s}^{-1}$ ) is given by eq X

$$\left( \frac{d[\text{C}=\text{O}]}{dt} \right)_t = k_s [\text{O}_3]_s [\text{SAM}]_0 (1 - f_t) \quad (\text{X})$$

where  $k_s$  is the second-order reaction rate constant ( $\text{cm}^2 \text{ s}^{-1}$  molecules $^{-1}$ ) and  $f_t$  is the fraction of the SAM that has reacted with ozone at time  $t$  (which can be estimated based on the ratio

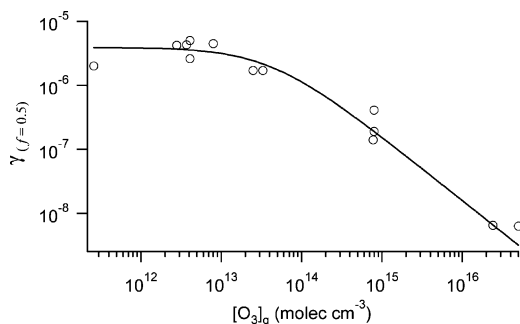


**Figure 9.** Calculated reaction probabilities for the oxidation of C3= at the time when half of the SAM has been oxidized ( $f = 0.5$ ) as a function of the gas-phase ozone concentration. The solid line is the least-squares fit of the data to eq XII.

of  $\text{abs}(\text{C}=\text{C})_t$  to the final absorption  $\text{abs}(\text{C}=\text{C})_\infty$ ). Combining eqs IX and X gives

$$\left(\frac{d[\text{C}=\text{O}]}{dt}\right)_t = k_s[\text{SAM}]_0(1-f_t)\frac{[\text{O}_3]_g[\text{S}]}{[\text{O}_3]_g + B} \quad (\text{XI})$$

Substituting eq V in eq XI and rearranging the latter provides a new expression for the reaction probability (equation XII), which contains two unknowns,  $B$  and  $k_s$

$$\gamma = \frac{k_s[\text{SAM}]_0(1-f_t)}{\sqrt{RT/2\pi M}} \times \frac{[\text{S}]}{[\text{O}_3]_g + B} \quad (\text{XII})$$

For consistency over the large range of  $\text{O}_3$  concentrations used in these studies (which covers 5 orders of magnitude), the experimental data were analyzed by calculating values of  $\gamma$  at the point where half of the SAM had reacted (i.e.,  $f_t = 0.5$ ) using eq VI. The values obtained for  $\gamma_{(f=0.5)}$  are plotted as a function of  $[\text{O}_3]_g$  in Figure 9. The best fit value for  $B$  is  $(4 \pm 3) \times 10^{13}$  molecules  $\text{cm}^{-3}$ , and the best fit value for  $k_s$  is  $(2 \pm 1) \times 10^{-17}$   $\text{cm}^2$  molecules $^{-1}$  s $^{-1}$  ( $1\sigma$ ). A value of  $f_t$  of 0 or 0.25 instead of 0.5 does not alter significantly the values obtained for  $B$  or  $k_s$ .

The calculated  $B$  for the present system is about an order of magnitude larger than the value obtained for ozone on benzo[a]pyrene (BaP)-coated soot ( $3.6 \times 10^{12}$  molecules  $\text{cm}^{-3}$ ; the  $K$  value reported in that study is equal to  $B^{-1}$ ).<sup>27</sup> Because  $B$  is the ratio of the desorption rate constant to that for adsorption, its magnitude is related to the strength of binding of  $\text{O}_3$  to the substrate. Soot is known to have free radical sites<sup>61</sup> with which ozone is expected to strongly interact, leading to smaller rates of desorption relative to adsorption and hence smaller values of  $B$  as is the case for soot compared to the SAMs. However, the  $B$  value from these studies is smaller than that for anthracene adsorbed on either water ( $2.1 \times 10^{15}$   $\text{cm}^3$  molecule $^{-1}$ ) or an aqueous octanol solution ( $5.1 \times 10^{14}$   $\text{cm}^3$  molecule $^{-1}$ ),<sup>22</sup> implying that ozone is more strongly adsorbed on the SAMs in the present study than on the polycyclic aromatic hydrocarbon (PAH) coating on aqueous solutions. In the latter case, significant amounts of water vapor are present, and this may alter the surface and hence the strength of binding of  $\text{O}_3$  to it. Indeed, Pöschl et al.<sup>27</sup> observed water competed with  $\text{O}_3$  for surface sites on the BaP-coated soot.

The value obtained for  $k_s$  is very similar to the rate constant reported previously for the surface reaction of ozone with benzo[a]pyrene on soot aerosols,  $(2.6 \pm 0.8) \times 10^{-17}$   $\text{cm}^2$  molecule $^{-1}$  s $^{-1}$ ,<sup>27</sup> and with anthracene adsorbed at the air–water interface,  $2.6 \times 10^{-17}$   $\text{cm}^2$  molecule $^{-1}$  s $^{-1}$ .<sup>22</sup> The value for  $k_s$  reported here is consistent with Knudsen cell data on the uptake of ozone

on silica particles coated with C8=<sup>25</sup> An initial uptake coefficient for  $\text{O}_3$  of  $(7 \pm 2) \times 10^{-5}$  was reported. However, the data in Figure 5 of the Usher et al.<sup>25</sup> paper show a small, but continuing, uptake of  $\text{O}_3$  with production of gas-phase products as indicated by a peak at  $m/e = 29$ . We estimate from these data that the uptake coefficient during this time is  $\sim 7 \times 10^{-6}$ . The gas-phase ozone concentration in those experiments was  $1.9 \times 10^{11}$  molecules  $\text{cm}^{-3}$ . Applying eq XII with our values of  $B$  and  $k_s$ , a SAM concentration of  $3 \times 10^{14}$  molecules  $\text{cm}^{-2}$ , and assuming  $f = 0.1$ , an uptake coefficient of  $7 \times 10^{-6}$  is calculated using the Langmuir–Hinshelwood mechanism for the experimental conditions of Usher et al.<sup>25</sup> Given the approximations made, this is in very good agreement with the slower uptake of ozone at longer reaction times that they observed.

The values of  $k_s$  reported for the reaction of surface-adsorbed ozone with BaP-coated soot, anthracene on aqueous solutions, and SAMs on a solid substrate are surprisingly similar, suggesting that there is a common, rate-determining step. All three organics have electron-rich  $\pi$  systems, and the formation of weak  $\pi$  complexes between ozone and alkenes has been reported at low temperatures,<sup>62–64</sup> suggesting that perhaps partial electron transfer is a key step in the oxidation.

The residence time of ozone on the surface is equal to  $k_d^{-1}$  ( $= [B \times k_a]^{-1}$ ). The adsorption rate constant  $k_a$  is given by eq XIII

$$k_a \text{ (cm}^3 \text{ molecules}^{-1} \text{ s}^{-1}\text{)} = \frac{S_0 \sqrt{\frac{RT}{2\pi M}}}{[\text{S}]} \quad (\text{XIII})$$

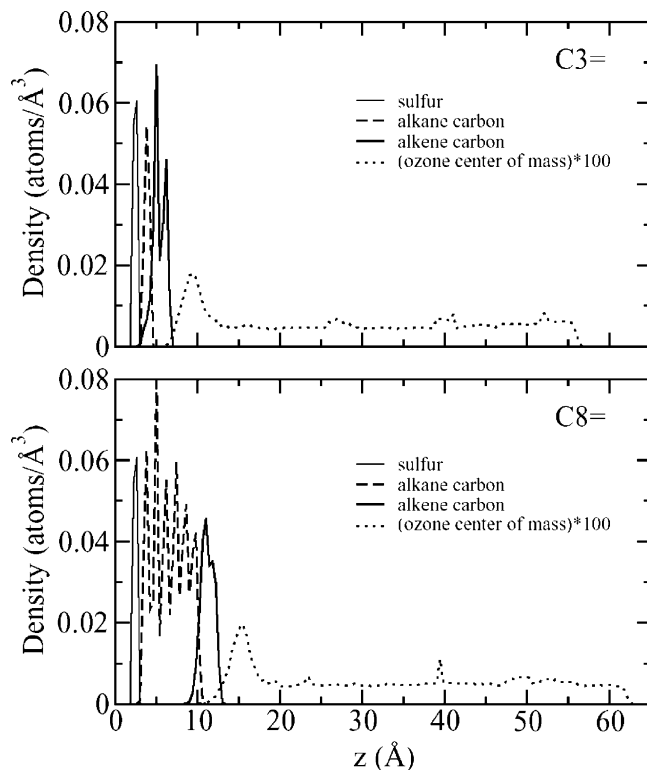
where  $S_0$  is the average uptake coefficient. Ammann et al.<sup>60</sup> have demonstrated that as long as the surface coverage of the adsorbed gas species ( $\text{O}_3$  in our case) is well below saturation, its uptake coefficient equals  $S_0$  and is independent of its gas-phase concentration. Moise and Rudich<sup>16</sup> report uptake coefficients for  $\text{O}_3$  on C3= and C8= of  $2.7 \times 10^{-4}$  and  $1.7 \times 10^{-4}$ , respectively, which were independent of  $[\text{O}_3]_g$  over the range of  $10^9$  to  $10^{11}$  molecules  $\text{cm}^{-3}$ . Thus, it seems that these measured uptake coefficients at very low ozone concentrations likely represent the surface accommodation of these SAMs with respect to  $\text{O}_3$ . This conclusion is further supported by the  $B$  value obtained from our experimental data ( $\sim 4 \times 10^{13}$  molecules  $\text{cm}^{-3}$  s $^{-1}$ ), which indicates a fractional surface coverage by ozone (i.e.,  $[\text{O}_3]_s/[\text{S}]$ ; eq IX) on the order of only 0.3% at  $[\text{O}_3]_g = 10^{11}$  molecules  $\text{cm}^{-3}$ . Use of an average uptake coefficient of  $2 \times 10^{-4}$  and surface density of adsorption sites of  $\sim 5 \times 10^{14}$  gives a value for  $k_a$  of  $\sim 4 \times 10^{-15}$   $\text{cm}^3$  s $^{-1}$  molecule $^{-1}$  for  $\text{O}_3$  at 298 K (eq XIII). On the basis of these values of  $B$  and  $k_a$ , a value of 0.15 s $^{-1}$  is calculated for  $k_d$ , indicating a residence time of ca. 7 s. This relatively long residence time is of the same order of magnitude as the residence times reported by Pöschl et al.<sup>27</sup> for  $\text{O}_3$  on BaP-coated soot.

In the gas phase, a typical reaction probability ( $\gamma_g$ ) for ozone with terminal alkenes (e.g., 1-hexene) is about  $3 \times 10^{-8}$ , based on rate constant of  $1 \times 10^{-17}$   $\text{cm}^3$  molecules $^{-1}$  s $^{-1}$  and a diffusion-controlled rate constant of  $\sim 3 \times 10^{-10}$   $\text{cm}^3$  molecule $^{-1}$  s $^{-1}$ .<sup>3</sup> Substitution of this reaction probability in eq V suggests that at  $[\text{O}_3]_g \sim 10^{15}$  molecules  $\text{cm}^{-3}$  oxidation of a SAM with a surface density of  $3.8 \times 10^{14}$  molecules  $\text{cm}^{-2}$  should be complete after  $\sim 30$  min, about 10 times slower than the time observed experimentally (Figure 7). This discrepancy increases with decreasing ozone concentrations; other studies on the heterogeneous oxidation of unsaturated alkenes by ozone have indicated similar trends.<sup>13,15,16,22,25,27</sup> Unlike the case of very

**TABLE 1: Collision Rates( $s^{-1} \times \text{ppm}^{-1} \times \text{cm}^{-2}$ ) of Ozone with the C3= and C8= SAMs**

system	theoretical ozone-surface <sup>a</sup>	simulation ozone-surface <sup>b</sup>	residence time (ps)	simulation ozone-alkene <sup>c</sup>	collision lifetime (ps)
C3=	$2.2 \times 10^{17}$	$2.1 \times 10^{17}$	14	$16 \times 10^{17}$	0.19
C8=	$2.2 \times 10^{17}$	$1.7 \times 10^{17}$	17	$20 \times 10^{17}$	0.23

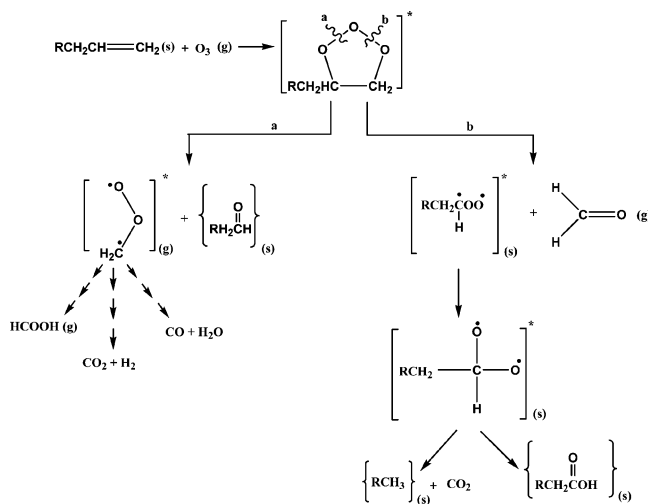
<sup>a</sup> Rates calculated based on gas-phase collision theory. <sup>b</sup> Surface collision defined as ozone molecule entering and exiting the vicinity of the SAM (see text). <sup>c</sup> Alkene collision defined as distance of approach  $\leq 4$  Å between center of masses of ozone and double bond.



**Figure 10.** Simulated density profiles of sulfur (thin solid line), alkane carbon (dashed line), alkene carbon (solid line), and ozone (dotted line) in (a) 1-propenethiolate and (b) 1-octenethiolate SAMs–ozone systems.

porous organic surfaces,<sup>15</sup> the present SAMs form a relatively packed and rigid surface layer (Figures 3 and 5), and therefore an enhanced reaction probability due to significant ozone trapping between the SAMs chains is not likely. This assumption is supported by depth profiles (Figure 10) from the MD simulations for such SAMs, showing a very limited penetration of the ozone molecules into the SAM.

To check whether the enhancement in the oxidation rate of the SAMs by ozone observed in the present study is due to an enhancement in reaction probability or in residence time on the terminal alkenes, molecular dynamic simulations of the interaction of ozone with similar SAMs were conducted. Table 1 summarizes the collision rates of ozone with the surface as a whole and with the terminal alkene in particular as calculated either from gas-phase collision theory or from the MD simulations. In these simulations, collision between an  $\text{O}_3$  molecule and the surface was defined as an  $\text{O}_3$  molecule that goes below a threshold value in the  $z$  dimension and then returns above that threshold value. The  $z$  threshold selections of 15 Å for the C3= SAM system and 20 Å for the C8= SAM system were made to be greater than the maximum  $z$  coordinate of the ozone center of mass observed while an ozone molecule was adsorbed to the SAM surface. A collision of  $\text{O}_3$  with an alkene group was defined as a distance of 4 Å or less between the ozone center of mass and the center of the double bond. Four angstroms was selected as the cutoff distance based on ab initio

**SCHEME 1: Schematic Diagram of Heterogeneous Ozonolysis of Alkenes<sup>a</sup>**

<sup>a</sup> The labels (s) and (g) represent surface and gas-phase species, respectively.

calculations suggesting that a stable complex is formed on the reaction pathway at a separation of 3.291 Å.<sup>64</sup> The rates obtained for  $\text{O}_3$  collision with the surface are slower than its collision rates with the terminal alkene by factors of 8 and 12 for C3= and C8=, respectively (Table 1). This apparent difference between collision rates of  $\text{O}_3$  with the surface and with alkene groups is due to inelastic collisions of  $\text{O}_3$  with the surface, yielding multiple collisions with the terminal alkenes in every collision with the SAM surface. The MD simulations indicate a residence time of  $\text{O}_3$  near the C3= and C8= interface of about 14 and 17 ps, respectively. This residence time is due to van der Waals interaction between the SAM and the  $\text{O}_3$  molecules.

Thus, both the experimental data and the MD simulations support a Langmuir–Hinshelwood type mechanism for the interaction of gaseous ozone and the unsaturated SAMs. However, the multiple encounters of an ozone molecule with the terminal alkenes upon each collision with the surface, as suggested by the MD simulations (about a factor of 10), can only account for part of the observed enhancement in oxidation rate. The residence time of ozone on the surface as calculated from the experimental data,  $\sim 7$  s, is much longer than the time obtained from the MD simulations ( $\sim 17$  ps). This discrepancy suggests that the adsorption of ozone on the surface involves not just van der Waals attraction but also chemisorption.<sup>62–64</sup>

**Products and Mechanism.** The products of the oxidation of alkenes by ozone are expected to be aldehydes and the Criegee intermediates (Scheme 1).<sup>3,11,12</sup> In the gas phase, the Criegee intermediate is known to decompose to form stable products such as  $\text{CO}_2$  and free radicals such as OH or to rearrange to a carboxylic acid. The increase in the carbonyl band in the  $1700 \text{ cm}^{-1}$  region during the reaction was accompanied by a small simultaneous increase in the absorption around  $3400 \text{ cm}^{-1}$ , suggesting the formation of a carboxylic acid on the surface. To probe this further, the oxidized SAMs were exposed

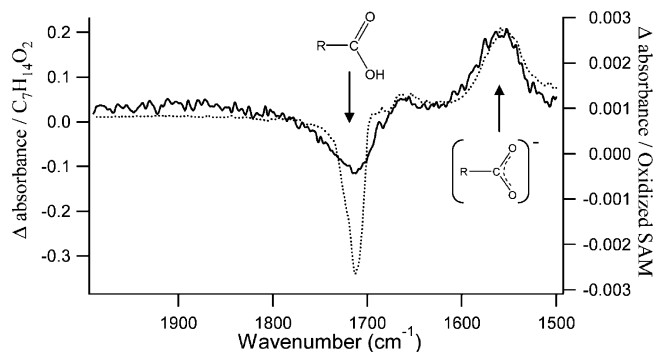


**Figure 11.** Changes in the absorption spectra of oxidized C8= (solid line) and pentanoic acid (dotted line) upon exposure to  $\text{NH}_3$  vapors, showing the conversion of the carboxylic acid ( $\sim 1710\text{ cm}^{-1}$ ) to carboxylate ( $1555\text{ cm}^{-1}$ ). Spectra were obtained by ratiating the single beam spectra after exposure to the ones before exposure to  $\text{NH}_3$ .

to gaseous  $\text{NH}_3$ , which reacts quickly with acids to form an ammonium salt; in separate experiments we showed that the reaction with aldehydes was much slower under these conditions. As seen in Figure 11 when the SAMs were exposed to  $\text{NH}_3$ , the C=O peak decreases sharply and a new absorption band appears at  $1555\text{ cm}^{-1}$ , indicating the formation of carboxylate ions. Similar results were observed upon exposure of an authentic sample of pentanoic acid to gaseous  $\text{NH}_3$  (Figure 11). Thus, carboxylic acids are formed in the ozone reaction with vinyl-terminated SAMs.

As discussed earlier, the larger width of the carbonyl peak for the reacted C3= may be in part due to the presence of a significant amount of aldehyde in addition to the carboxylic acid.

However, the presence of aldehydes cannot be definitively established based on the ATR spectra of the reacted films.

Further insight into the mechanism can be obtained from studies of the gas phase products. Cavity ring-down spectroscopy (CRDS) was used for real-time detection of gas phase products released during the ozonolysis of C3=, C8=, and C8 SAMs (Figure 12). In the control experiments on the ozonolysis of C8 SAMs, no HCHO or HCOOH gas-phase products were observed in CRDS spectra except for a small background from outgassing of the CRDS chamber walls (Figure 12a). On the contrary, ozonolysis of alkene-terminated SAMs under identical conditions reproducibly resulted in considerably larger signals from HCHO in agreement with the expected mechanism of the terminal C=C bond cleavage by  $\text{O}_3$  (Scheme 1, path b). For example, characteristic HCHO bands are clearly visible in both C8= and C3= spectra. The amount of HCHO produced in ozonolysis of C3= and C8= SAMs is comparable, suggesting the primary ozonide splitting pattern is not too different in these two films. No significant signal from HCOOH was observed in either case; an upper limit for the formation of HCOOH is about 10% of that of HCHO. The small yield observed for the formation of HCOOH is consistent with two possibilities. First, the decomposition of the primary ozonide mainly follows pathway b in Scheme 1, releasing HCHO to the gas phase and leaving the Criegee intermediate on the surface. This rearranges and stabilizes to form the carboxylic acid, which was confirmed to be present on the surface by reaction with  $\text{NH}_3$ . A second possibility is that the Criegee intermediate released to the gas phase in pathway a of Scheme 1 rapidly decomposes to form  $\text{CO}_2$ ,  $\text{CO}$ ,  $\text{H}_2$ , and  $\text{H}_2\text{O}$  rather than isomerizing to HCOOH. The latter occurs, for example, in the gas-phase ozone-propene reaction where yields of ( $\text{CO} + \text{CO}_2$ ) were measured to be 52% compared to a yield of 11% for formic acid.<sup>65</sup> The wall loss for

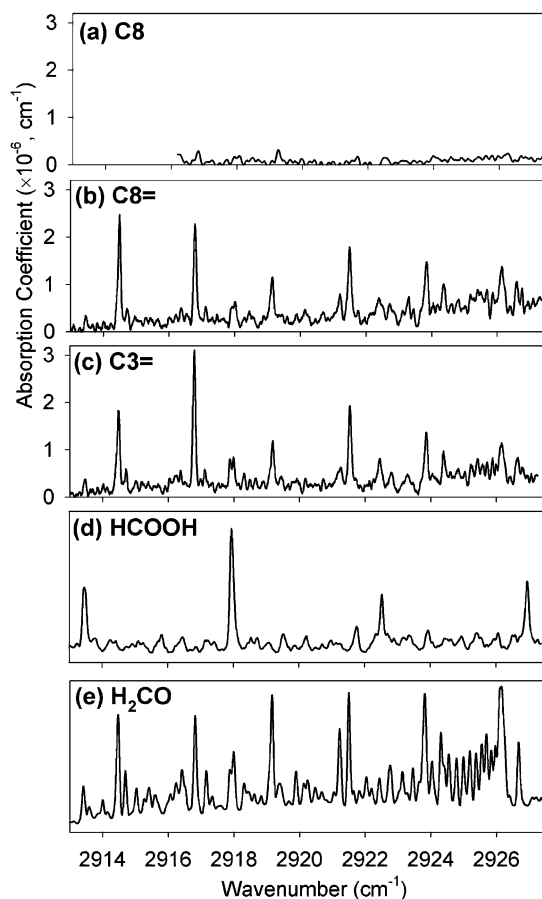


**Figure 12.** CRDS spectra obtained during the reaction of  $\text{O}_3$  ( $\sim 10^{14}$  molecules  $\text{cm}^{-3}$ ) of (a) C8, (b) C8=, and (c) C3= (y axis is absorption coefficient in  $\text{cm}^{-1}$ ). Also shown are (d) the reference optoacoustic spectrum of  $\text{HC(O)OH}$  vapor and (e) the reference spectrum of HCHO downloaded from the National Solar Observatory database convoluted to  $0.1\text{ cm}^{-1}$  resolution. (Note: stronger lines in this spectrum are saturated.)

HCOOH is expected to be larger than that for HCHO, which may also contribute to the lower apparent HCOOH yield.

The products observed here can be compared to those reported by Rudich and co-workers<sup>17</sup> and Grassian and co-workers.<sup>25</sup> In the former case, HCHO was observed as the major gas-phase product of both the C3= and C8= oxidations, with a yield of about 50% of the ozone reacted. Smaller amounts of  $\text{CO}_2$ , and CO in the case of C3= were also measured. Formic acid was only observed in the C3= oxidation and only at total pressures below 80 Torr; even then, the yield was less than 5%. If small amounts of formic acid were released to the gas phase, the formation of an aldehyde group on the surface would be expected (Scheme 1, path a). The broader carbonyl peak we observed in the ATR spectra of oxidized C3= compared to oxidized C8= suggests that there could be a higher HCOOH yield for C3= than that for C8= as reported by Rudich and co-workers,<sup>17</sup> although it was below the IR-CRDS detection limit.

Usher et al.<sup>25</sup> used  $^{13}\text{C}$  solid-state NMR to search for products on the surface. Although signals due to the alkene carbons decreased upon reaction, no signals due to aldehyde or carboxylic acid groups were observed. They concluded that oxygen-containing products did not remain on the surface and proposed that the reaction proceeded via formation of gas-phase HCHO and a Criegee biradical on the surface; the latter was hypothesized to have decomposed to generate gas-phase  $\text{CO}_2$  and a surface alkane. Such decompositions may be more important

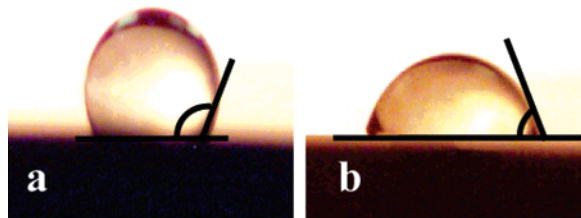


**Figure 13.** A 1  $\mu\text{L}$  water droplet resting on a C8= monolayer (a) before and (b) after exposure to  $\text{O}_3$  ( $8 \times 10^{14}$  molecules $^{-1}$  cm $^3$ ). Contact angles are marked with black lines.

under the low-pressure conditions of their Knudsen cell than at atmospheric pressure under which the present experiments were carried out.

Conversion of the alkene to carboxylic acids and aldehydes upon reaction with ozone is expected to make the surface more hydrophilic. The contact angles of water droplets on the SAM-coated crystal were measured before and after exposure to ozone (Figure 13). After oxidation at higher concentrations of  $\text{O}_3$  ( $\sim 10^{15}$  molecules cm $^{-3}$ ), the contact angle of both the C3= and C8= (Figure 13) SAMs decreased by about  $20^\circ$ , whereas relatively little change was observed for the saturated C8 SAM. Both the values of the initial contact angles and the amplitude of their reduction upon oxidation are in good agreement with previous studies on similar SAMs.<sup>16,17</sup>

At the CH-stretching frequency range of the ATR-FTIR spectra (data not shown), a small decrease in the  $\text{CH}_2$  bands of the unsaturated SAMs is observed upon ozone oxidation (no such changes are observed when saturated C8 is used). Because ozone has very low reactivity toward saturated alkanes, these results suggest the formation of OH during the ozonolysis. However, the same trends were observed when conducting the experiments in the presence of excess ethane, indicating that increasing disorder of the unsaturated monolayers during their oxidation, rather than secondary OH oxidation, is the dominant factor affecting the absorption bands in this region. This is in agreement with previous studies on heterogeneous oxidation of alkenes by ozone<sup>15,17,20,21</sup> and suggests that the excess energy of the intermediate left attached to the surface is quickly damped before it decomposes.

Interestingly, during experiments with  $\text{O}_3$  concentrations above  $5 \times 10^{16}$  molecules cm $^{-3}$ , the absorption of the carbonyl band continues to rise slowly even after most of the C=C bonds appear to have been consumed (Figure 14). This may be due to oxidation of alkene bonds in the interior of what appears to be polymer aggregates seen on the surface by AFM (Figure 5) and/or secondary oxidation.

### Conclusions and Atmospheric Implications

The present work demonstrates the utility of ATR-FTIR to monitor heterogeneous oxidation of organic surfaces (SAMs in this case) by ozone. One of the advantages of using this unintrusive spectroscopic technique is that it permits real-time monitoring of both reactants and products on the surface under ambient temperature and pressure. These spectra show that upon exposure to ozone the terminal alkene groups of these SAMs are quickly oxidized to form carbonyls. Some of these carbonyl groups are present as carboxylic acid as indicated by the formation of ammonium salt upon exposure of the oxidized sample to  $\text{NH}_3$  vapor. The relatively broad carbonyl peak observed in the ATR-FTIR spectra of oxidized C3= relative to oxidized C8= suggests the presence of a significant amount of aldehyde in addition to the carboxylic acid. Cavity ring down spectroscopy indicates the formation of gas-phase HCHO in

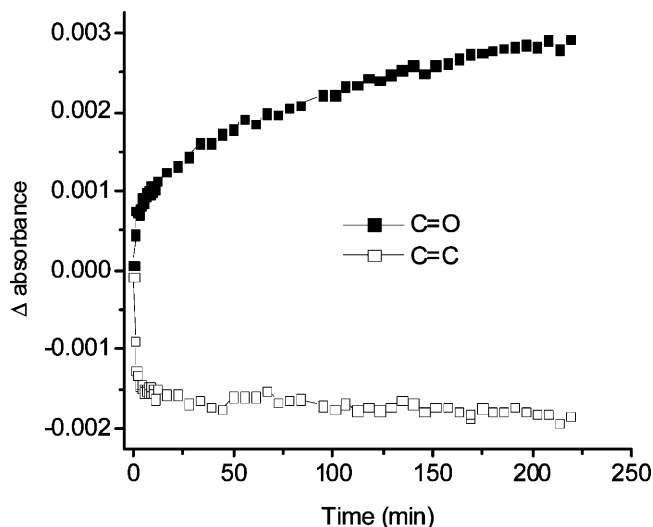


**Figure 14.** Change in absorbance at the C=O band (solid squares) and C=C band (open squares) of C3= SAM as a function of exposure time to  $6 \times 10^{16}$  molecules cm $^{-3}$  of ozone.

significantly higher yield than that for HCOOH. This can be a result of preferable formation of formaldehyde during the decomposition of the primary ozonide or because of rapid decomposition of the Criegee intermediate rather than stabilization to form HCOOH.

The formation of more polar species on the surface contributes to an increase in surface hydrophilicity, as indicated by the observed decrease in the contact angle of the water droplet on the unsaturated SAM after oxidation (by  $\sim 20^\circ$ ). Similar oxidation processes are expected to occur on organic aerosols during their residence in the atmosphere. Thus, the optical properties of some organic aerosols and their potential to become active CCN under atmospheric conditions may also depend on their residence time in the atmosphere, the concentration of atmospheric oxidants, and the rate of such heterogeneous oxidation reactions.

An interesting picture of the oxidative processing kinetics of organic aerosols is beginning to emerge as experiments have been combined with molecular dynamics computer simulations.<sup>15,24</sup> In the case of SAMs, which are model systems for organic molecules adsorbed on urban surfaces and solid particles (e.g., mineral dust),<sup>25</sup> the oxidation by ozone occurs via a Langmuir–Hinshelwood type mechanism involving a rapid equilibration between gaseous and adsorbed ozone and a slower surface reaction between ozone and the terminal alkene group of the SAMs. The best fit to the experimental data yields a Langmuir constant ( $B$ ) of  $(4 \pm 3) \times 10^{13}$  molecules cm $^{-3}$  and a second-order rate constant for the surface oxidation reaction ( $k_s$ ) of  $(2 \pm 1) \times 10^{-17}$  cm $^2$  molecule $^{-1}$  s $^{-1}$ . These values are similar to those reported previously for the heterogeneous reactions of ozone with benzo[a]pyrene on soot aerosols<sup>27</sup> and anthracene on water or aqueous octanol solutions.<sup>22</sup> One important implication of the fact that the heterogeneous ozonolysis of surface alkene (present work) and aromatic compounds<sup>22,27</sup> follows a Langmuir–Hinshelwood type mechanism is that the use of a simple reaction probability independent of the ozone concentration to calculate the loss of the organic or uptake of ozone is not appropriate. A more complex approach that represents the molecular level mechanism must be used when incorporating laboratory data for such heterogeneous reactions into atmospheric models.

Although the MD simulations predict a residence time of  $\sim 17$  ps for ozone on the surface, the experimental data suggest a

much longer residence time, of the order of several seconds. This discrepancy between simulations and experiments, and the long residence time suggested by the latter, suggests that chemisorption (e.g., through the formation of a  $\pi$  complex) plays a significant role in these heterogeneous processes. Both the van der Waals attraction, which leads to multiple "encounters" of ozone with the surface during a collision, and the chemisorption likely contribute to the rapid oxidation of the SAM relative to what is expected based on analogous gas-phase reactions. For example, in urban atmospheres, where terminal alkenes account for a significant fraction of the unsaturated compounds, ozone levels are on the order of 80 ppb. On the basis of the values of  $B$  and  $k_s$  obtained in the present study, an initial oxidation rate for such thin alkene films is calculated (using eq XI) to be on the order of  $5 \times 10^{-4}$  molecules  $s^{-1}$  per surface site, indicating a lifetime for the SAM of about 0.6 h. However, considering a typical rate constant<sup>3</sup> for the reaction of ozone with gaseous aliphatic alkene of about  $1 \times 10^{-17}$   $cm^3$  molecule<sup>-1</sup>  $s^{-1}$  (e.g., 1-butene), a lifetime for gas-phase terminal alkenes of about 15 h is obtained. It should be noted that this rapid oxidation of unsaturated SAMs on surfaces could also lead to artifacts in sampling such organics on particles under some conditions, as has been observed for PAH, for example.<sup>66</sup>

Despite their importance in the atmosphere, heterogeneous reactions on organic aerosols are not yet considered in most atmospheric models. This is mainly due to the large diversity of organic species present in atmospheric aerosols as well as a significant lack of information regarding the kinetics and mechanisms of such reactions. This study demonstrates the importance of real-time monitoring of reactions at surfaces involved in such heterogeneous reactions and the potential of using both ATR-FTIR and MD simulations to enhance our understanding of these important surface processes.

**Acknowledgment.** We are grateful to the National Science Foundation for support of a Collaborative Research in Chemistry award (CHE-0209719) and an Environmental Molecular Sciences Institute (CHE-0431512) under which this research was carried out, Professor Jim Rutledge for assistance with the contact angle measurements, and Lee Moritz and Jorg Meyer for technical assistance. S.A.N. thanks the Research Corporation for a Research Innovation Award.

## References and Notes

- (1) *Change Climate 2001: The Scientific Basis*; Houghton, J. T., Ding, Y., Griggs, D. J., Noguer, M., van der Linden, P. J., Dai, X., Maskell, K., Johnson, C. A., Eds.; Intergovernmental Panel on Climate Change, Cambridge University Press: Cambridge, 2001.
- (2) Ramanathan, V.; Crutzen, P. J.; Kiehl, J. T.; Rosenfeld, D. *Science* **2001**, *294*, 2119.
- (3) Finlayson-Pitts, B. J.; Pitts, J. N., Jr. *Chemistry of the Upper and Lower Atmosphere: Theory, Experiments and Applications*; Academic Press: San Diego, 2000.
- (4) Jacobson, M. C.; Hansson, H. C.; Noone, K. J.; Charlson, R. J. *Rev. Geophys.* **2000**, *38*, 267.
- (5) Murphy, D. M.; Thomson, D. S.; Mahoney, T. M. *J. Science* **1998**, *282*, 1664.
- (6) Husar, R. B.; Shu, W. R. *J. Appl. Meteorol.* **1975**, *14*, 1558.
- (7) Tervahattu, H.; Hartonen, K.; Kerminen, V.-M.; Kupiainen, K.; Aarnio, P.; Koskentalo, T.; Tuck, A. F.; Vaida, V. *J. Geophys. Res.* **2002**, *107*, AA41.
- (8) Tervahattu, H.; Juhanaja, J.; Kupiainen, K. *J. Geophys. Res.* **2002**, *107*, Art. No. 4319.
- (9) Rudich, Y. *Chem. Rev.* **2003**, *103*, 5097.
- (10) Weingartner, E.; Burtscher, H.; Baltensperger, U. *Atmos. Environ.* **1997**, *31*, 2311.
- (11) Atkinson, R.; Arey, J. *Atmos. Environ.* **2003**, *37*, S197.
- (12) Atkinson, R.; Arey, J. *Chem. Rev.* **2003**, *103*, 4605.
- (13) Lai, C. C.; Yang, S. H.; Finlayson-Pitts, B. J. *Langmuir* **1994**, *10*, 4637.
- (14) de Gouw, J. A.; Lovejoy, E. R. *Geophys. Res. Lett.* **1998**, *25*, 931.
- (15) Wadia, Y.; Tobias, D. J.; Stafford, R.; Finlayson-Pitts, B. J. *Langmuir* **2000**, *16*, 9321.
- (16) Moise, T.; Rudich, Y. *J. Geophys. Res.* **2000**, *105*, 14667.
- (17) Thomas, E. R.; Frost, G. J.; Rudich, Y. *J. Geophys. Res.* **2001**, *106*, 3045.
- (18) Morris, J. W.; Davidovits, P.; Jayne, J. T.; Jimenez, J. L.; Shi, Q.; Kolb, C. E.; Worsnop, D. R.; Barney, W. S.; Cass, G. *Geophys. Res. Lett.* **2002**, *29*.
- (19) Smith, G. D.; Woods, E.; DeForest, C. L.; Baer, T.; Miller, R. E. *J. Phys. Chem. A* **2002**, *106*, 8085.
- (20) Moise, T.; Rudich, Y. *J. Phys. Chem. A* **2002**, *106*, 6469.
- (21) Eliason, T. L.; Aloisio, S.; Donaldson, D. J.; Cziczko, D. J.; Vaida, V. *Atmos. Environ.* **2003**, *37*, 2207.
- (22) Mmereki, B. T.; Donaldson, D. J. *J. Phys. Chem. A* **2003**, *107*, 11038.
- (23) Thornberry, T.; Abbatt, J. P. D. *Phys. Chem. Chem. Phys.* **2004**, *6*, 84.
- (24) Vieceli, J.; Ma, O. L.; Tobias, D. J. *J. Chem. Phys. A* **2004**, *108*, 5806.
- (25) Usher, C. R.; Michel, A. E.; Grassian, V. H. *Chem. Rev.* **2003**, *103*, 4883.
- (26) Uosaki, K.; Quayum, M. E.; Nihonyanagi, S.; Kondo, T. *Langmuir* **2004**, *20*, 1207.
- (27) Pöschl, U.; Letzel, T.; Schauer, C.; Niessner, R. *J. Phys. Chem. A* **2001**, *105*, 4029.
- (28) Diamond, M. L.; Gingrich, S. E.; Fertuck, K.; McCarry, B. E.; Stern, G. A.; Billeck, B.; Grift, B.; Brooker, D.; Yager, T. D. *Environ. Sci. Technol.* **2000**, *34*, 2900.
- (29) Gingrich, S. E.; Diamond, M. L.; Stern, G. A.; McCarry, B. E. *Environ. Sci. Technol.* **2001**, *35*, 4031.
- (30) Finlayson-Pitts, B. J.; Wingen, L. M.; Sumner, A. L.; Syomin, D.; Ramazan, K. A. *Phys. Chem. Chem. Phys.* **2003**, *5*, 223.
- (31) Sagiv, J. *J. Am. Chem. Soc.* **1980**, *102*, 92.
- (32) DeMore, W. B.; Sander, S. P.; Golden, D. M.; Hampson, R. F.; Kurylo, M. J.; Howard, C. J.; Ravishankara, A. R.; Kolb, C. E.; Molina, M. J. *Chemical Kinetics and Photochemical Data for Use in Stratospheric Modeling, Evaluation No. 12*; Jet Propulsion Laboratory: Pasadena, CA, 1997; Vol. JPL Publ. No. 97-4.
- (33) Harrick, N. J. *Internal Reflection Spectroscopy*; Interscience Publishers: New York, 1967.
- (34) Ulman, A. *ACS Symp. Ser.* **1991**, No. 447, 144.
- (35) Mar, W.; Klein, M. L. *Langmuir* **1994**, *10*, 188.
- (36) Ulman, A. *Chem. Rev.* **1996**, *96*, 1533.
- (37) Allara, D. L.; Atul N. P.; F., R. *Langmuir* **1995**, *11*, 2357.
- (38) Porter, M. D.; Bright, T. B.; Allara, D. L.; Chidsey, C. E. D. *J. Am. Chem. Soc.* **1987**, *109*, 3559.
- (39) Tobias, D. J.; Tu, K.; Klein, M. L. *J. Chem. Phys.* **1997**, *94*, 1482.
- (40) MacKerell, A. D.; Bashford, D.; Bellott, M.; Dunbrack, R. L.; Evanseck, J. D.; Field, M. J.; Fischer, S.; Gao, J.; Guo, H.; Ha, S.; Joseph-McCarthy, D. J.; Kuchnir, L.; Kuczera, K.; Lau, F. T. K.; Mattos, C.; Michnick, S.; Ngo, T.; Nguyen, D. T.; Prodhom, B.; Reiher, W. E.; Roux, B.; Schlenkrich, M.; Smith, J. C.; Stote, R.; Straub, J.; Watanabe, M.; Wiorkiewicz-Kuczera, J.; Yin, D.; Karplus, M. *J. Phys. Chem B* **1998**, *102*, 3586.
- (41) Meerts, W. L.; Stolte, S.; Dymanus, A. *Chem. Phys.* **1977**, *19*, 467.
- (42) Mack, K. M.; Muentner, J. S. *J. Chem. Phys.* **1977**, *66*, 5278.
- (43) Trambarulo, R.; Gosh, S. N.; Burrus, C. A.; Gordy, W. *J. Chem. Phys.* **1953**, *21*, 851.
- (44) Brooks, B. R.; Brucoleri, R. E.; Olafson, B. D.; States, D. J.; Swaminathan, S.; Karplus, M. *J. Comput. Chem.* **1983**, *4*, 187.
- (45) Martyna, G. J.; Tuckerman, M. E.; Tobias, D. J.; Klein, M. L. *Mol. Phys.* **1996**, *87*, 1117.
- (46) Ryckaert, J. P.; Ciccotti, G.; Berendsen, H. C. J. *Comput. Chem.* **1977**, *23*, 327.
- (47) Andersen, H. C. *J. Comput. Chem.* **1983**, *52*, 24.
- (48) Roeges, N. P. G. *A Guide to the Complete Interpretation of Infrared Spectra of Organic Structures*; John Wiley & Sons: New York, 1994.
- (49) Flinn, D. H.; Guzonas, D. A.; Yoon, R. H. *Colloids Surf., A* **1994**, *87*, 163.
- (50) Angst, D. L.; Simmons, G. W. *Langmuir* **1991**, *7*, 2236.
- (51) Maoz, R.; Sagiv, J. *J. Colloid Interface Sci.* **1984**, *100*, 465.
- (52) Netzer, L.; Iscovici, R.; Sagiv, J. *Thin Solid Films* **1983**, *100*, 67.
- (53) Wasserman, S. R.; Tao, Y. T.; Whitesides, G. M. *Langmuir* **1989**, *5*, 1074.
- (54) Dordi, B.; Schonherr, H.; Vancso, G. J. *Langmuir* **2003**, *19*, 5780.
- (55) Banga, R.; Yarwood, J.; Morgan, A. M.; Evans, B.; Kells, J. *Langmuir* **1995**, *11*, 4393.
- (56) Banga, R.; Yarwood, J.; Morgan, A. M.; Evans, B.; Kells, J. *Thin Solid Films* **1996**, *285*, 261.

- (57) Iler, R. K. *The Chemistry of Silica*; Wiley: New York, 1979; Chapter 6.
- (58) Zhuravlev, L. T. *Langmuir* **1987**, 3, 316.
- (59) Adamson, A. W.; Gast, A. P. *Physical Chemistry of Surfaces*, 6th ed.; Wiley-Interscience: New York, 1997.
- (60) Ammann, M.; Pöschl, U.; Rudich, Y. *Phys. Chem. Chem. Phys.* **2003**, 5, 351.
- (61) Chughtai, A. R.; Atteya, M. M. O.; Kim, J.; Konowalchuck, B. K.; Smith, D. M. *Carbon* **1998**, 36, 1573.
- (62) Bailey, P. S.; Ward, J. W.; Hornish, R. E. *J. Am. Chem. Soc.* **1971**, 93, 3552.

- (63) Hull, L. A.; Hitsatsune, I. C.; Heicklen, J. *J. Am. Chem. Soc.* **1972**, 94, 4856.
- (64) Gillies, C. W.; Gillies, J. Z.; Suenram, R. D.; Lovas, F. J.; Kraka, E.; Cremer, D. *J. Am. Chem. Soc.* **1991**, 113, 2412.
- (65) Disselkamp, R. S.; Dupuis, M. *J. Atmos. Chem.* **2001**, 40, 231.
- (66) Schauer, C.; Niessner, R.; Pöschl, U. *Environ. Sci. Technol.* **2003**, 37, 2861.
- (67) Katrib, Y.; Martin, S. T.; Hung, H. M.; Rudich, Y.; Zhang, H. Z.; Slowik, J. G.; Davidovits, P.; Jayne, J. T.; Worsnop, D. R. *J. Phys. Chem. A* **2004**, 108, 6686.